Pyroelectric energy converter for harvesting waste heat: Simulations versus experiments

Raylene C. Moreno, Brian A. James, Ashcon Navid, Laurent Pilon *

Mechanical and Aerospace Engineering Department, Henry Samueli School of Engineering and Applied Science, University of California, Los Angeles, Los Angeles, CA 90095, USA

ABSTRACT

This paper is concerned with numerical simulations of a pyroelectric converter for direct energy conversion of waste heat into electricity. The simulated prototypical device consisted of a hot and cold source separated by a series of vertical microchannels supporting pyroelectric thin films made of co-polymer P(VDF-TrFE) and undergoing the Olsen cycle. A piston was used to vertically oscillate a working fluid back and forth between the thermal sources. The experimental device was instrumented with thermocouples and a pressure sensor. The two-dimensional transient mass, momentum, and energy equations were solved numerically using finite element methods to determine the local and time-dependent temperature at various locations inside the device microchannels. The operating frequency varied from 0.025 to 0.123 Hz and the working fluid was 1.5 or 50 cSt silicone oil. Good agreement was found between the simulated and experimentally measured local mean temperatures for both working fluids at all operating frequencies considered. The local temperature swings were underestimated slightly for 50 cSt silicone oil and significantly more for 1.5 cSt silicone oil. Overall, this study confirms our previous numerical results. Moreover, this numerical model could be used to design and operate the next generation of pyroelectric energy converters based on oscillatory convective heat transfer.

© 2012 Elsevier Ltd. All rights reserved.

1. Introduction

Waste heat is a necessary by-product of all thermodynamic cycles implemented in power, refrigeration, and heat pump devices. In 2009, energy losses corresponded to more than 50% of the primary energy consumed in the United States [1]. The necessity to develop more energy efficient engineering systems has brought significant attention to waste heat energy harvesting devices [2–4]. Unfortunately, small Carnot efficiencies have hindered the development of such devices. Organic Rankine cycles and Stirling engines have been utilized to convert waste heat into mechanical work [2,3]. Particularly, Stirling engines have been used in heat pump, cryogenic refrigeration, and air liquefaction applications [3]. Additionally, thermoelectric devices utilize the Seebeck effect to convert directly a steady-state temperature difference at the junction of two dissimilar metals or semiconductors into electrical energy [4]. Alternatively, pyroelectric energy converters directly convert thermal energy into electricity using time-dependent temperature oscillations combined with a cycle in the displacement-electric field diagram [5–11].

Prototypical pyroelectric energy converters based on laminar oscillatory convective heat transfer consist of a series of vertical microchannels supporting pyroelectric elements positioned between a hot and a cold source [5–10,12]. A working fluid typically oscillates through microchannels between the hot and cold sources to produce the time-dependent temperature oscillations in the pyroelectric material necessary to generate electricity. The devices assembled to date have demonstrated the feasibility of the technology, but their design has not been optimized for maximum performance [13].

This paper aims to experimentally validate a numerical model simulating a prototypical pyroelectric energy converter [13,14]. To do so, it compares results from detailed numerical simulations with those obtained experimentally by Nguyen et al. [12] for various operating conditions. Such a numerical tool could then be used to design and optimize the device in a rapid and cost-effective manner.

2. Current state of knowledge

2.1. Pyroelectric energy conversion

Fig. 1 shows the isothermal unipolar hysteresis curves in the electric displacement D and electric field E diagram at temperatures T_{hot} and T_{cold} typical of pyroelectric materials. The D–E loops move counter-clockwise upon isothermal cycling of the electric field across the material. Above the Curie temperature T_{Curie},

* Corresponding author. Tel.: +1 310 206 5598; fax: +1 310 206 4830.
  E-mail address: pilon@seas.ucla.edu (L. Pilon).

Nomenclature

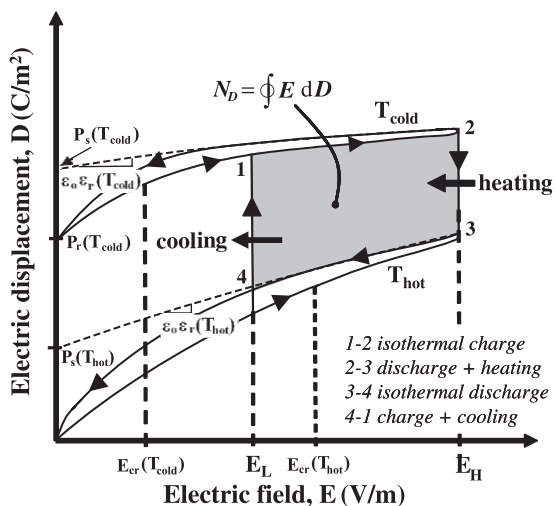|				
A_c	cross-sectional area of fluid flow for one channel, m^2		Q_{in}	heat transfer rate into pyroelectric converter, W
A_{ht}	area of heater per unit depth ($=2L_{ht}$), m		Q_{out}	heat transfer rate out of pyroelectric converter, W
A_{hx}	area of heat exchanger per unit depth ($=2L_{hx}$), m		S	piston stroke length, m
A_p	cross-sectional area of piston, m^2		S'	amplitude of working fluid in microchannel, m
c_p	specific heat, J/kg K		t	time, s
d	channel depth, m		T	temperature, °C
D	electric displacement, C/m^2		T_C	temperature of cold source, °C
E	electric field, V/m		T_{Curie}	Curie temperature, °C
f	frequency, Hz		T_H	temperature of hot source, °C
g	gravity, m^2/s		$T_{i,max}$	maximum temperature at location i, °C
k	thermal conductivity, W/m K		$T_{i,min}$	minimum temperature at location i, °C
L	total length of wall, m		ΔT	temperature swing ($=T_{i,max} - T_{i,min}$), °C
L_{cold}	length of heat exchanger section, m		w	microchannel half-width, m
L_{hot}	length of heater section, m		x	transverse coordinate in (x,z) coordinate system
L_{ht}	length of heater, m		z	vertical coordinate in (x,z) coordinate system
L_{hx}	length of heat exchanger, m			
L_m	length of mica plate, m		*Greek symbols*	
L_{PE}	length of pyroelectric element, m		α	thermal diffusivity ($=k/\rho c_p$), m^2/s
N	number of internal walls supporting pyroelectric elements		ν	kinematic viscosity, m^2/s
			ρ	density, kg/m^3
N_D	energy density, J/L/cycle		τ	period of oscillation ($=1/f$), s
$\vec{n}$	normal vector			
p	pressure, Pa		*Subscripts*	
p_0	atmospheric pressure at free surface, Pa		f	refers to working fluid
P_D	power density, W/L		i	refers to location i
P_S	spontaneous polarization, C/m^2		m	refers to mica plate
$q_{in,exp}$	experimental heat input at heater, W		p	refers to piston
$q_{out,exp}$	experimental heat output at heat exchanger, W		PE	refers to pyroelectric element
$q'_{in,num}$	numerical input heat flux per unit depth at heater, W/m		w	refers to walls
$q'_{out,num}$	numerical output heat flux per unit depth at heat exchanger, W/m			

Fig. 1. Electric displacement versus electric field for a typical pyroelectric material at different temperatures. The Olsen cycle is represented by the process 1–4.

pyroelectric materials undergo a phase transition from ferroelectric to paraelectric. Then, the D–E loop is nearly linear and the spontaneous polarization P_S vanishes.

The Olsen cycle (or Ericsson cycle) [5] consists of two isothermal and two iso-electric field processes. It is performed by alternatively bringing a pyroelectric element (PE), consisting of a pyroelectric film sandwiched between two electrodes, in thermal contact with a hot and cold source at T_{hot} and T_{cold} while the electric field is cycled between E_L and E_H. The area enclosed within points 1–4 represents the electrical energy produced by the material undergoing the Olsen cycle per unit volume of pyroelectric materials and per cycle. It is expressed in J/L/cycle and defined as $N_D = \oint E dD$ [9].

Multistaging and heat regeneration are two design strategies which can significantly enhance the efficiency and power output of the Olsen cycle [8,9]. On the one hand, multistaging consists of placing multiple pyroelectric elements from the cold to the hot source with increasing Curie temperature. On the other hand, heat regeneration consists of placing the PE in contact with a working fluid that oscillates between the hot and cold sources. Then, the heat required to increase the temperature of the PE or the oscillating working fluid is regenerated back and forth between them rather than being lost to the heat sink. Furthermore, it was established that the Olsen cycle with heat regeneration can theoretically achieve the Carnot efficiency between a hot and cold reservoir in a pyroelectric energy conversion [8,15]. In practice, leakage current through the PEs, heat losses to the surroundings, friction, and sensible thermal energy prohibit reaching the Carnot efficiency [8,15].

Several prototypical pyroelectric energy converters were assembled and operated by Olsen et al. [5–7] in the early 1980's. The devices produced 1 and 40 mW electrical power at efficiencies of 0.4%. Olsen and co-workers operated their devices using PZST as the pyroelectric material and silicone oil as the working fluid with viscosity ranging between 50 and 200 cSt. The working fluid was oscillated vertically using a step motor with a piston stroke length of 7.8–10 cm. The temperature of the cold and hot sources were 145 and 178 °C, respectively. Alumina microchannels ensured

laminar flow of the working fluid over the PEs and reduced axial heat conduction between the hot and cold sources. Additionally, Olsen et al. [8] built a multistage device with different grades of PZST. This device achieved a maximum power density of 33 W/L of pyroelectric material when operated at frequency 0.26 Hz and had a maximum efficiency of 1.05% at 0.14 Hz, corresponding to 12% of the Carnot efficiency between 150 and 180 °C. Olsen et al. [10] also constructed a device using inexpensive 30–70 μm thick poly (vinylidene fluoride–trifluoroethylene) [73/27 P(VDF-TrFE)] films. The device was operated at temperatures between 20 and 90 °C and achieved an energy density of 30 J/L/cycle. Unfortunately, the local temperatures and pressure at different locations in these devices were not reported.

More recently, Nguyen et al. [12] assembled and operated an instrumented pyroelectric converter that performed the Olsen cycle using 60/40 P(VDF-TrFE) as the pyroelectric material. Mica stacks were used to create microchannels and 1.5 cSt and 50 cSt silicone oils were used as the working fluid. Temperature was measured at five locations inside the device along with pressure. A maximum energy density of 130 J/L/cycle of pyroelectric material was obtained at 0.061 Hz with PE temperature oscillating between 69.3 and 87.6 °C. A maximum power density of 10.7 W/L was obtained at 0.12 Hz between 70.5 and 85.3 °C [12]. In addition, using 1.5 cSt silicone oil resulted in larger temperature swings than those obtained with 50 cSt silicone oil for given frequency, hot and cold source temperatures T_H and T_C [12]. This larger temperature swing was obtained for smaller heat inputs which should increase both the energy density and the device efficiency.

2.2. Numerical simulations

Construction and testing of pyroelectric energy converters can be costly and time-consuming. Therefore, simulation tools have been previously developed in order to numerically predict the performance of prototypical pyroelectric energy converters. The first numerical simulations of a pyroelectric device were reported by Olsen et al. [16] to determine the heat transfer rate and temperature variations of the microchannel walls for peak-to-peak stroke lengths of 2.8, 5.1, and 8.5 cm and frequencies between 0 to 0.6 Hz. The numerical simulations only solved the energy conservation equation under the assumptions that (1) microchannel walls were made of alumina, (2) fluid flow was one-dimensional, oscillatory, laminar, and fully developed, thus producing parabolic velocity profiles across the microchannels, (3) axial heat conduction along the walls of the device was negligible, and (4) the hot and cold heat exchangers were placed immediately above and below the PE material, respectively, and maintained at constant temperatures. Olsen et al. [8] determined that the numerically predicted and experimentally measured input and output heat transfer rates were in good agreement for all frequencies when the stroke length was smaller than 2.8 cm. However, results became increasingly inaccurate for larger and preferable stroke lengths.

More recently, Vanderpool et al. [14] performed two-dimensional numerical simulations of a prototypical pyroelectric converter experimentally assembled by Olsen et al. [8]. The 2D transient mass, momentum, and energy conservation equations were solved simultaneously in order to compute the pumping power and to accurately predict the temperature oscillations of the PE materials. The purpose of these simulations was to identify important design and operating parameters in the pyroelectric device that would lead to larger power output and higher thermodynamic efficiency. The authors concluded that: (1) the mass, momentum, and energy equations must be solved simultaneously to accurately predict the local temperature in the device, (2) the numerically predicted thermodynamic efficiency fell within 29% of experimental

data [8] at all frequencies and optimum stroke length of 3.9 cm, (3) the efficiency was very small at larger frequencies ($f > 0.1$ Hz) due to a faster increase in heat input relative to the generated electrical power, and (4) reducing the heat capacity of the working fluid and the PE resulted in increased device efficiency.

Finally, Navid et al. [13] used the numerical framework developed by Vanderpool et al. [14] to investigate the effects of geometric parameters and properties of actual working fluids on the device performance. The authors established that shortening the device improved its performance and enabled it to operate more efficiently at higher frequencies. This resulted in a maximum efficiency of 2.2% with a power density of 40.7 W/L using 50 cSt silicone oil and PZST subjected to the Olsen cycle with temperature between 145 and 185 °C and electric field between 4 and 28 kV/cm. Additionally, reducing the viscosity of the working fluid from 50 cSt to 1.5 cSt, as commercially available, further improved the maximum efficiency to 5.2%, corresponding to a power density of 38.4 W/L and 55% of Carnot efficiency between 145 and 185 °C. Note that these simulations accounted for pumping power required to overcome fluid friction in the simulated test section but ignored frictions between the cylinder and the piston oscillating the working fluid.

In previous studies [14,16], detailed numerical simulations were validated against experimental data for "global quantities" such as the overall heat input and output [16] or the device efficiency [14]. The relatively good agreement may hide large discrepancies in some local variables used in designing the device. By contrast, this paper aims to validate the simulation tool previously developed [13,14] against local temperature measurements recently collected in a prototypical pyroelectric energy converter [12].

3. Analysis

3.1. Pyroelectric energy converter

3.1.1. Experimental apparatus

The prototypical pyroelectric energy converter, based on the Olsen cycle, constructed by Nguyen et al. [12], consisted of a thermal and an electrical sub-system. The thermal sub-system was used to create a time-dependent temperature oscillation by heating the PE to a maximum temperature T_{hot} and cooling it to a minimum temperature T_{cold}. The electrical sub-system controlled the electric field applied to the PEs to perform the Olsen cycle (Fig. 1). It also collected the charges generated during the cycle. The device consisted of 37 equally spaced PE assemblies supported by mica plates placed inside the device to form 38 microchannels. Fig. 2(a) shows a schematic of the cross-section of the device in which the stack of PE assemblies was located between the electrical heater and the cold heat exchanger. Each PE assembly consisted of one pyroelectric film made of 60/40 P(VDF-TrFE) with electrodes sandwiched between two mica plates with 10×10 mm^2 windows cut out to expose each side of the PE to the working fluid oscillating in the microchannels [12]. The latter were 330 μm wide and 40.6 mm long. Mica was chosen as the wall material due to its low thermal conductivity and high dielectric strength. The PE assemblies were joined to form the PE stack, which was enclosed in a Teflon cylinder to guide the vertical motion of the fluid and to act as a thermal insulator. The channels were filled with the working fluid and a piston-cylinder assembly was used to oscillate the working fluid vertically between the cold and hot sources. Moreover, the piston assembly featured adjustable stroke length S and operating frequency f. The optimal stroke length was chosen to be $S = 4.7$ cm corresponding to the distance separating the cold heat exchanger to the heat source. Larger stroke lengths would result in excessive heat losses while smaller ones would reduce the temperature swing experienced by the PE.
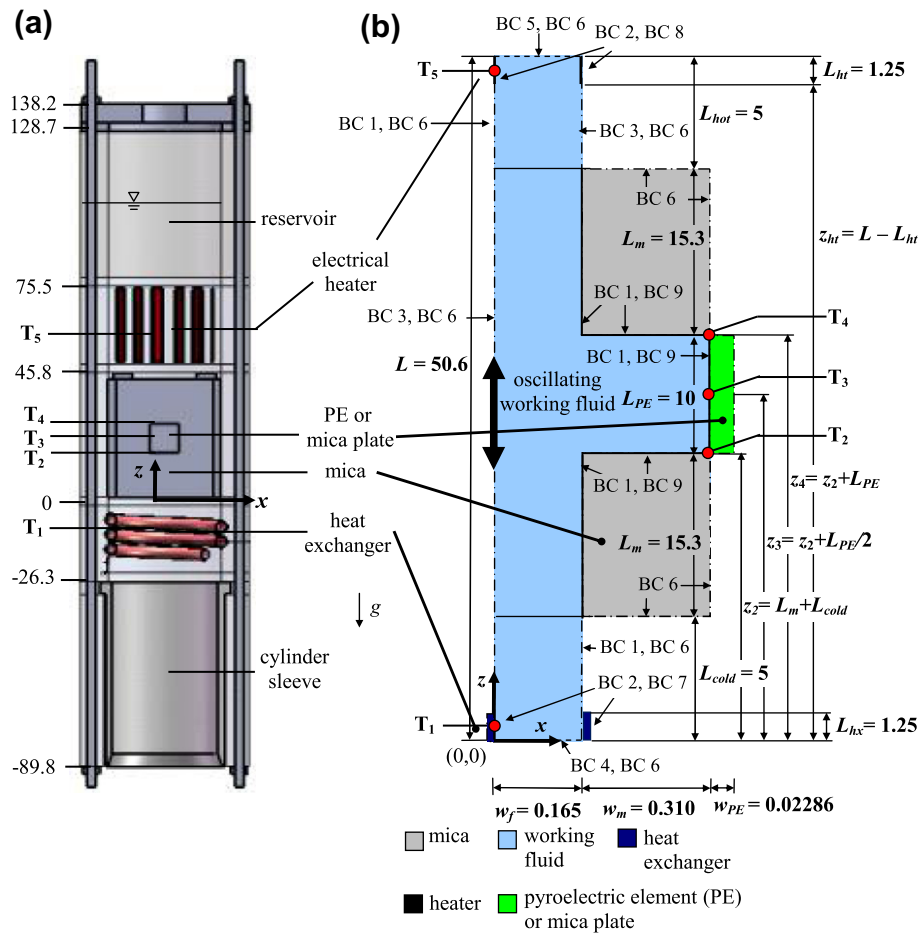
Fig. 2. Schematic (a) of the experimental pyroelectric energy converter [12], and (b) of the computational domain along with the coordinate system, dimensions (all dimensions in mm), and boundary conditions (BC).

Below the microchannels, the cold reservoir featured a copper coil serving as a heat exchanger to cool the working fluid to an average temperature T_C. Similarly, the fluid in the hot reservoir above the stack was heated by a thin copper band to an average temperature T_H. The local temperatures T_2 to T_4 (Fig. 2) were measured using thermocouples placed in a channel adjacent to the channel supporting the PE. This channel contained a mica plate as a substitute for the PE in order to limit the risk of the thermocouple discharging and/or short circuiting the PE [12]. The temperature of the heat exchanger (T_1) and heater (T_5) were measured in the center of the cylinder below and above the channels.

3.1.2. Numerical model

Fig. 2(b) shows the computational domain of the simulated pyroelectric converter along with the dimensions, coordinate system, and the applied boundary conditions. The same assumptions as those made by Vanderpool et al. [14] and Navid et al. [13] were made in the present study. In particular, the working fluid was treated as an incompressible Newtonian fluid with constant properties. In addition, the fluid flow was assumed to be two-dimensional since the microchannel depth was much larger than its width. By virtue of symmetry, only half of a microchannel was simulated. The hot and cold sources were both numerically simulated as line sources operating at constant heat flux $q'_{in,num}$ and $q'_{out,num}$, respectively. In order to decrease the number of elements in the finite element meshes and therefore decrease the computational cost, the heater and cold heat exchanger simulated had shorter lengths than in the experimental device. However, the same net heat input and output as those measured experimentally were imposed.

Each microchannel had a total height $L = 50.6$ mm. In addition, the length of the top and bottom mica wall plates was denoted by $L_m = 15.3$ mm. The cold reservoir containing the heat exchanger had a height of $L_{cold} = 5$ mm. Each of the two line sources which served as the heat exchanger had a length of $L_{hx} = 1.25$ mm and were located on opposite sides at the bottom of the cold reservoir. This resulted in a total cold heat exchanger length of 2.5 mm. Similarly, the hot reservoir was of length $L_{hot} = 5$ mm. The heater had length $L_{ht} = 2.5$ mm and was located at height $z_{ht} = L - L_{ht} = 49.35$ mm. The temperature of the cold and hot reservoirs denoted by T_1 and T_5 and were measured at location $z_1 = L_{hx}/2 = 0.625$ mm and $z_5 = L_{ht}/2 = 49.975$ mm at the centerline of the channel. The locations of the thermocouples measuring the temperatures at the bottom (T_2), middle (T_3), and top (T_4) of the PE were denoted by $z_2 = (L_m + L_{cold}) = 20.3$ mm, $z_3 = (z_2 + L_{PE}/2) = 25.3$ mm, and $z_4 = (z_2 + L_{PE}) = 30.3$ mm, respectively. They were placed at the PE/fluid interface along $x = w_f + w_m$ as illustrated in Fig. 2(b). The mica plates had a total width $w_m = 310$ μm, while the half-width of the channel and the PE, were $w_f = 165$ μm and $w_{PE} = 22.86$ μm, respectively (Fig. 2(b)). The location of the top surface of the oscillating piston was given by $z_p = -S[1 + cos(2\pi ft)]$ so that when the piston was at its maximum height of $z_p = 0$, a fluid particle at the top of the heating band $z = L$ would travel down to the bottom of the PE ($z = z_2$) when the piston was at its lowest point $z_p = -2S$.

Finally, the electric power generated by the converter was not modeled in the present study. Kandilian et al. [17] modeled the energy generated during the Olsen cycle. It was successfully validated for single crystal PMN-PT and PZN-PT and ceramics PLZT [17–19]. However, the model ignored leakage current which can

be significant in P(VDF-TrFE) particularly under high temperature and electric field.

3.2. Governing equations

The two-dimensional (2D) transient mass and momentum conservation equations for an incompressible Newtonian fluid with constant properties in Cartesian coordinates were solved to determine the velocity components and pressure field of the working fluid. They are expressed as [20],

$$\frac{\partial u_f}{\partial x} + \frac{\partial v_f}{\partial z} = 0 \tag{1}$$

$$\frac{\partial u_f}{\partial t} + u_f \frac{\partial u_f}{\partial x} + v_f \frac{\partial u_f}{\partial z} = -\frac{1}{\rho_f}\frac{\partial p_f}{\partial x} + v_f\left(\frac{\partial^2 u_f}{\partial x^2} + \frac{\partial^2 u_f}{\partial z^2}\right) \tag{2}$$

$$\frac{\partial v_f}{\partial t} + u_f \frac{\partial v_f}{\partial x} + v_f \frac{\partial v_f}{\partial z} = -\frac{1}{\rho_f}\frac{\partial p_f}{\partial z} - g + v_f\left(\frac{\partial^2 v_f}{\partial x^2} + \frac{\partial^2 v_f}{\partial z^2}\right) \tag{3}$$

where ρ_f and v_f are the density and kinematic viscosity of the working fluid, respectively. The x- and z-components of the velocity vector are denoted by u_f and v_f, respectively, while p_f is the local fluid pressure, and g is the gravitational acceleration (=9.81 m/s^2). Note that free convection was neglected by virtue of the fact that forced convection, driven by the piston, dominated the fluid flow and that the hot source was located above the cold source providing a stable temperature gradient in absence of piston oscillations [20].

The working fluid temperature $T_f(x,z,t)$ at location (x,z) and time t was determined by solving the transient, 2D energy equation given by [20],

$$\rho_f c_{p,f}\left(\frac{\partial T_f}{\partial t} + u_f \frac{\partial T_f}{\partial x} + v_f \frac{\partial T_f}{\partial z}\right) = k_f\left(\frac{\partial^2 T_f}{\partial x^2} + \frac{\partial^2 T_f}{\partial z^2}\right) \tag{4}$$

where $c_{p,f}$ and k_f are the fluid specific heat and thermal conductivity, respectively. These properties were also assumed to be constant. Additionally, viscous dissipation was neglected due to the fact that (i) the fluid velocity in the microchannels was small, (ii) the microchannels were relatively large, and (iii) the kinematic viscosity of silicone oil was not excessive at the mean operating temperature.

Finally, the transient 2D heat diffusion equation in the mica plates and in the P(VDF-TrFE) film that made up the microchannel walls was expressed as,

$$\rho_w c_{p,w}\frac{\partial T_w}{\partial t} = k_w\left(\frac{\partial^2 T_w}{\partial x^2} + \frac{\partial^2 T_w}{\partial z^2}\right) \tag{5}$$

where the subscript w refers to either the mica or to the PE material. Here also, the wall thermophysical properties were assumed to be isotropic and temperature-independent.

3.3. Initial and boundary conditions

Initially (at t = 0), the working fluid was at rest. Thus, for $0 \leqslant x \leqslant w_f$ when $0 \leqslant z \leqslant L$, and for $w_f \leqslant x \leqslant (w_f + w_m)$ when $z_2 \leqslant z \leqslant z_4$,

$$u_f(x,z,0) = v_f(x,z,0) = 0 \tag{6}$$

In addition, the initial fluid and structure temperatures were assumed to vary linearly between $z = L_{cold}$ and $z = L - L_{hot}$ corresponding to the top of the cold reservoir at temperature T_C and the bottom of the hot reservoir at temperature T_H, respectively. Furthermore, the fluid temperature in the hot and cold reservoirs containing the heater and cold heat exchanger was assumed to be uniform and equal to the wall temperature. Thus, for $0 \leqslant x \leqslant w_f + w_m + w_{PE}$,

$$T_f(x,z,0) = T_w(x,z,0) = \begin{cases} T_C & \text{for } 0 \leqslant z \leqslant L_{cold} \\ T_C + \dfrac{(T_H - T_C)(z - L_{cold})}{L - L_{hot} - L_{cold}} & \text{for } L_{cold} \leqslant z \leqslant L - L_{hot} \\ T_H & \text{for } L - L_{hot} \leqslant z \leqslant L \end{cases} \tag{7}$$

The mass, momentum, and energy equations were subject to the boundary conditions (BC) listed in Table 1 and illustrated in Fig. 2(b). Note that for the fluid-piston interface (BC 4) and for z < 0, the velocity of the working fluid was equal to the velocity of the piston given by $v_p = dz_p/dt = 2\pi f S \sin(2\pi ft)$. From mass conservation considerations and assuming that the fluid was incompressible, the velocity of the fluid at the bottom inlet of the channels was uniform and a sinusoidal function of time with amplitude $S' = (SA_p/[(N+1)A_c])$, where $A_p = 1.140$ mm^2 and $A_c = 0.319$ mm^2 are the cross-sectional area of the piston and of a single channel, respectively.

In the simulations, the numerical heat input and output per unit depth at the heater and heat exchanger, $q'_{in,num}$ and $q'_{out,num}$ were related to the experimental heat input of the heater, $Q_{in,exp}$, and output of the heat exchanger, $Q_{out,exp}$, by

$$q'_{in,num} = \frac{Q_{in,exp}}{2(N+1)A_{ht}} \quad \text{and} \quad q'_{out,num} = \frac{Q_{out,exp}}{2(N+1)A_{hx}} \tag{8}$$

where $(N+1)$ is the number of channels while $A_{ht} = 2L_{ht} = 2.5$ mm^2/mm and $A_{hx} = 2L_{hx} = 2.5$ mm^2/mm are the numerically simulated surface areas of the heater and cold heat exchanger, respectively for each channel and per unit depth. It is important to note that $Q_{in,exp}$ corresponds to the net experimental heat input reported by Nguyen et al. [12]. In other words, the numerical heat input was equivalent to the experimental one corrected for heat losses and thermal energy conversion into electricity by the Olsen cycle. Unfortunately, heat losses for experiments with 1.5 cSt silicone oil were not recorded experimentally. They were estimated to be 15% of heat inputs by analogy with heat losses observed experimentally with 50 cSt silicone oil. Table 2 summarizes the numerical and experimental heat input for different frequencies and working fluids.

Table 1
Boundary conditions (BC 1 to BC 5) associated with the 2D, transient mass and momentum conservation Eqs. (1)–(3) and (BC 6 to BC 9) with the 2D, transient energy conservation Eq. (4). BC 1 to BC 9 are illustrated in Fig. 2(b).

Boundary	Boundary condition	No.
Walls	$u_f(x,z,t) = 0$, $v_f(x,z,t) = 0$	BC 1
Heater and heat exchanger	$u_f(x,z,t) = 0$, $v_f(x,z,t) = 0$	BC 2
Channel centerline	$u_f(0,z,t) = \frac{\partial v_f}{\partial x}(0,z,t) = 0$	BC 3
Fluid–piston interface	$u_f(x,0,t) = 0$, $v_f(x,0,t) = 2\pi\, fS'\sin(2\pi ft)$	BC 4
Fluid–air interface	$p_f(x,L,t) - p_0 = \rho_f g S[1 - \cos(2\pi ft)]$	BC 5
Thermal insulation and centerline	$\vec{n}\cdot\left(\frac{\partial T}{\partial x}(x,z,t)\vec{i} + \frac{\partial T}{\partial z}(x,z,t)\vec{k}\right) = 0$	BC 6
Heat exchanger	$q'(x,z,t) = q'_{out} = -k_f\frac{\partial T_f}{\partial x}$	BC 7
Heater	$q'(x,z,t) = q'_{in} = -k_f\frac{\partial T_f}{\partial x}$	BC 8
Fluid–wall interface	$-k_f\frac{\partial T_f}{\partial x}(x,z,t) = -k_w\frac{\partial T_w}{\partial x}(x,z,t)$	BC 9

Table 2
Experimental heat transfer rate into ($Q_{in,exp}$) and out of ($Q_{in,exp}$) the pyroelectric converter along with the associated numerical boundary conditions $q'_{in,num}$ and $q'_{out,num}$ for operating frequencies between 0.025 and 0.123 Hz for 50 cSt and 1.5 cSt silicone oil.

Working fluid	50 cSt silicone oil			
	0.025 Hz	0.035 Hz	0.061 Hz	0.082 Hz
$Q_{in,exp}$ (W)	21.4	22.2	26.6	27.9
$Q_{out,exp}$ (W)	21.4	22.2	26.6	27.9
$q'_{in,num}$ (W/m)	113.2	116.8	140.0	146.8
$q'_{out,num}$ (W/m)	113.2	116.8	140.0	146.8
	1.5 cSt silicone oil			
	0.04 Hz	0.053 Hz	0.069 Hz	0.123 Hz
$Q_{in,exp}$ (W)	18.5	23.0	25.5	26.8
$Q_{out,exp}$ (W)	18.5	23.0	25.5	26.8
$q'_{in,num}$ (W/m)	97.53	121.1	134.0	141.2
$q'_{out,num}$ (W/m)	97.53	121.1	134.0	141.2

3.4. Properties

Table 3 summarizes the material properties of mica, P(VDF-TrFE), and 50 and 1.5 cSt silicone oils used in this study. The thermophysical properties of mica, 60/40 P(VDF-TrFE), and commercial 1.5 and 50 cSt silicone oils [21] were assumed to be constant over the temperature range simulated. Note that the kinematic viscosity v_f of 50 cSt silicone oil varies by as much as 55% between 45 °C and 105 °C. As a first order approximation, v_f was evaluated at the arithmetic mean temperature $\overline{T}_3$ of 74 °C, corresponding to the average temperature in the middle of the PE assembly. It was assumed to be constant and equal to 24.0 mm²/s for 50 cSt silicone oil and 0.89 mm²/s for 1.5 cSt silicone oil [21]. Similarly, the specific heat of the working fluid and P(VDF-TrFE), as well as the thermal conductivity of P(VDF-TrFE), were also estimated at 74 °C and obtained from Refs.[21–24]. Unfortunately, the densities of P(VDF-TrFE) and 50 and 1.5 cSt silicone oils, as well as the thermal conductivity of mica, were only available in the literature at or near room temperature [12,23]. In addition, the respective thermal conductivity of the working fluids was only available at 50 °C [21].

3.5. Method of solution

The transient 2D mass, momentum, and energy conservation equations (Eqs. (1)–(5)), along with their respective initial and boundary conditions (Table 1), were solved simultaneously using the finite element solver COMSOL 4.1 applying the Galerkin finite element method on structured triangular meshes. A Dell Precision 690 computer with eight 2.50 GHz processors, and 28 GB of RAM was used to perform the simulations. The internal time step was chosen to maintain numerical stability and never exceeded 0.1 s. The finite element mesh was refined in 40% increments until temperatures varied by less than 1.2% between subsequent mesh refinements. Oscillatory steady-state was assumed to be reached when the maximum and minimum values of temperatures T_1 to T_5 varied by less than 0.5% from one oscillation to the next. Finally, an overall energy balance analysis was systematically carried out

to ensure that energy was conserved for the entire computational domain.

3.6. Data analysis

The local temperatures were analyzed at the locations where temperatures T_1 to T_5 were measured experimentally [12] as illustrated in Fig. 2. This enabled direct comparison between the numerical predictions and experimental measurements [12]. For each location, the temperature swing ΔT_i at location i under oscillatory steady-state conditions was defined as $\Delta T_i = T_{i,max} - T_{i,min}$ where $T_{i,max}$ and $T_{i,min}$ are the maximum and minimum temperatures reached by $T_i(t)$ during one cycle. In addition, the arithmetic mean temperature $\overline{T}_i$ at location i was defined as $\overline{T}_i = (T_{i,max} + T_{i,min})/2$.

For comparison between numerical and experimental results, the local temperatures T_1 to T_5 were computed as a function of time at a given frequency f based on the net heat input and output given by Eq. (8). The sampling rate of the experimental measurements was 0.05 s. Numerical results were recorded at time intervals Δt such that $8\pi f\Delta t = \pi/2$ corresponding to sixteen data points per oscillation period. The numerical predictions for $\overline{T}_i$, $T_{i,min}$, $T_{i,max}$, and ΔT_i were also compared with experimental data reported by Nguyen et al. [12]. For simulations with 50 cSt silicone oil, the frequency ranged between 0.025 and 0.082 Hz while it varied between 0.04 and 0.123 Hz for 1.5 cSt silicone oil. Finally, the mica plate was replaced by the PE in the simulated channel to predict the actual PE temperatures T_2, T_3, and T_4 that could not be measured experimentally.

4. Results and discussion

4.1. Local temperatures

Fig. 3(a) to (e) compare the local temperatures T_1, T_2, T_3, T_4, and T_5 as functions of time predicted numerically and measured experimentally [12] at frequency 0.025 Hz for 50 cSt silicone oil. Fig. 3(a) shows that the mean temperature $\overline{T}_1$ and temperature swing ΔT_1 computed numerically were smaller than those measured experimentally by up to 17% and 16 °C, respectively. This was due to the fact that numerically the heat exchanger cooled the working fluid more effectively than experimentally. Indeed, in the numerical model, the heat exchanger was located at the bottom of each microchannel which allowed the working fluid to be cooled locally. However, experimentally, the heat exchanger was a copper coil wrapped inside the inner diameter of the Teflon cylinder enclosing the device. It was located in a large fluid reservoir below the mica plate stack (see Fig. 2(a)).

Similarly, the numerical predictions for $\overline{T}_2$ were slightly lower than the corresponding experimental measurements as a result of more effective local cooling provided by the heat exchanger. However, numerical predictions for $T_2(t)$, $\overline{T}_2$, and ΔT_2 (Fig. 3(b)) were significantly better than for their counterparts at location 1 (Fig. 3(a)) with $\overline{T}_2$ and ΔT_2 falling within 3% and 8 °C of experimental data, respectively. Similarly, good agreement (within 13%) was found for $T_3(t)$, $\overline{T}_3$, ΔT_3, $T_4(t)$, $\overline{T}_4$, and ΔT_4 between numerical

Table 3
Fluid and material properties used in the numerical simulations [12,21–24,28–30].

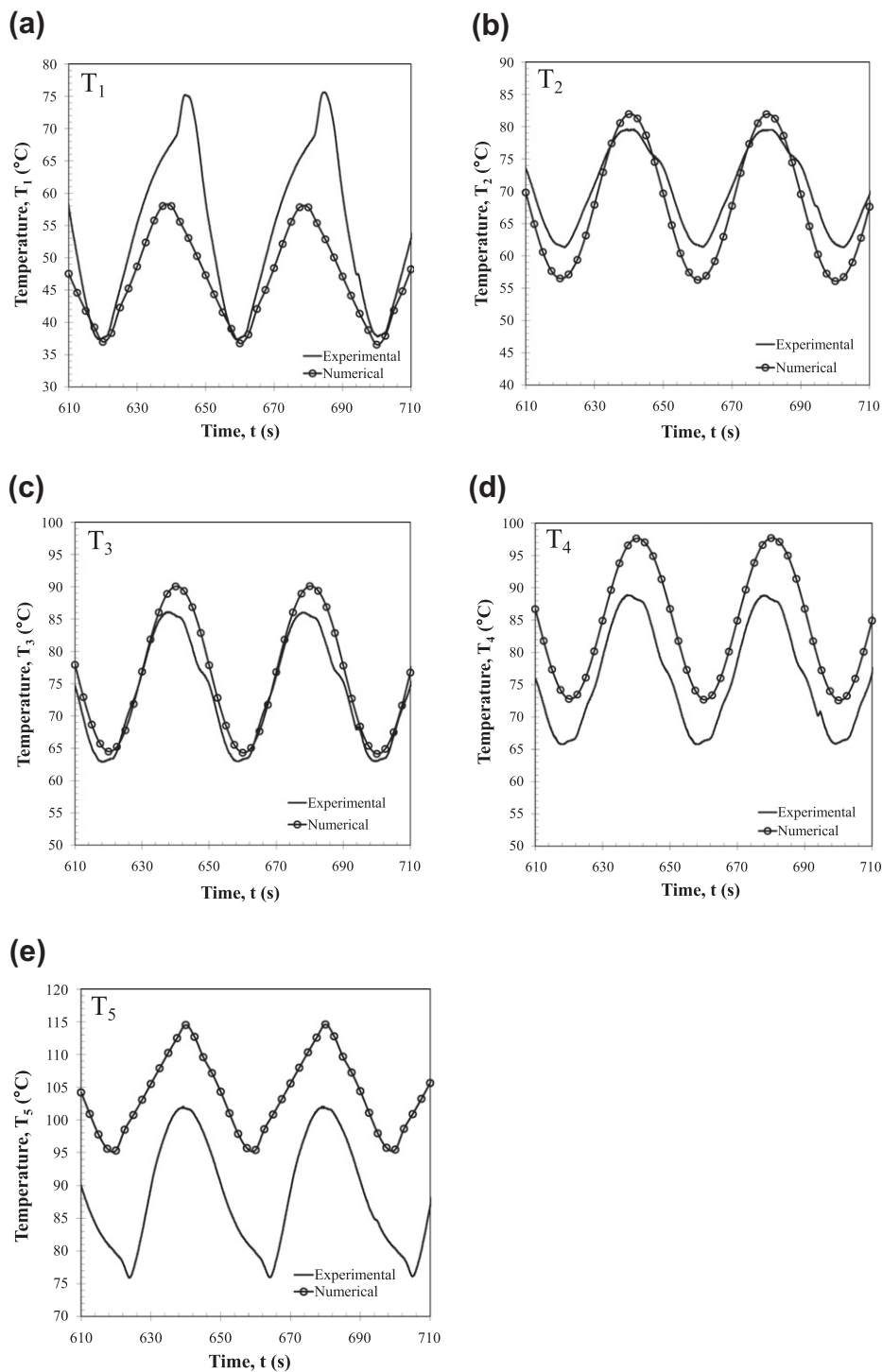| Property	1.5 cSt [21,28]	50 cSt [21,28]	P(VDF-TrFE) [23,24]	Mica [22,29,30]
ρ (kg/m³)	847 (25 °C)	957 (25 °C)	1879 (25 °C)	2131.4 (25 °C)
c_p (J/kg K)	1789 (74 °C)	1655 (74 °C)	2089 (74 °C)	890.02 (74 °C)
k (W/m K)	0.0966 (50 °C)	0.1428 (50 °C)	0.149 (74 °C)	0.3 (20 °C)
v_f (mm²/s)	0.89 (74 °C)	24 (74 °C)	–	–

Fig. 3. Computed and experimentally measured [12] temperatures as a function of time for frequency $f = 0.025$ Hz at the (a) heat exchanger T_1, (b) bottom of the mica plate substitute T_2, (c) middle of the mica plate substitute T_3, (d) top of the mica plate substitute T_4, and (e) heater T_5. The working fluid was 50 cSt silicone oil.

simulations and experimental results (Figs. 3(c) and (d)). Discrepancies could be explained by the fact that the experimental device contained thermocouples and electrical wires which obstructed the fluid flow in the microchannels and were not accounted for in the numerical simulations.

Moreover, numerical predictions for $T_5(t)$, $\overline{T}_5$, and ΔT_5 were larger than their corresponding experimental values for all frequencies. Numerically, the heater was more effective in heating the working fluid than experimentally. Indeed, experimentally, the heater was located in a large fluid reservoir above the mica stack

(see Fig. 2(a)). In the numerical model however, the heater was placed above each microchannel which provided a more uniform local heating of the working fluid. Overall, very good agreement was found between experimental measurements and numerical predictions for the device using 50 cSt slicone oil and operated at 0.025 Hz.

Finally, Fig. 4(a)–(e) compare the local temperatures T_1 to T_5 as functions of time predicted numerically and measured experimentally [12] at frequency 0.053 Hz for 1.5 cSt silicone oil. The experimentally measured mean temperatures $\overline{T}_i$ at all locations
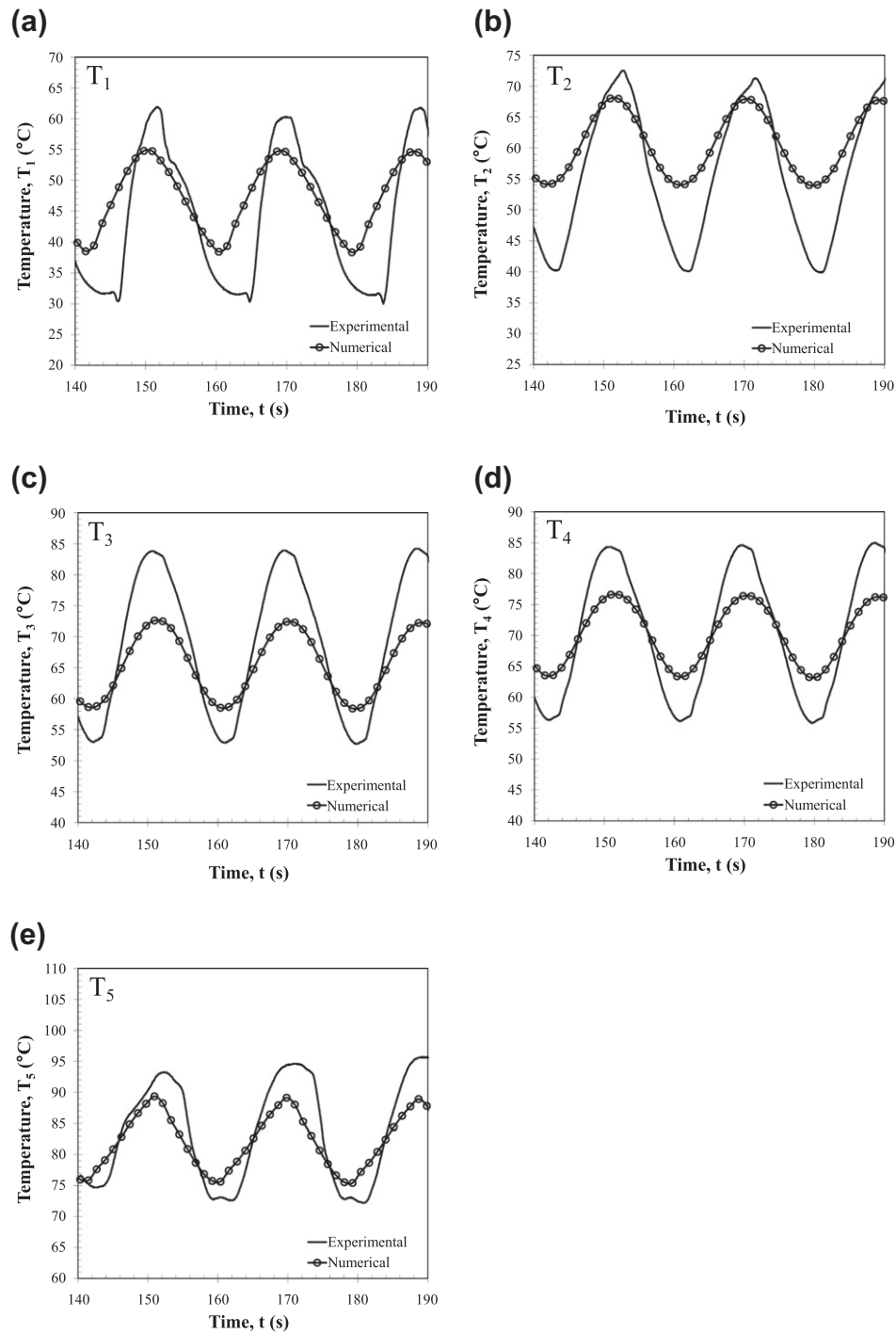
Fig. 4. Computed and experimentally measured [12] temperatures as a function of time for frequency $f = 0.053$ Hz at the (a) heat exchanger T_1, (b) bottom of the mica plate substitute T_2, (c) middle of the mica plate substitute T_3, (d) top of the mica plate substitute T_4, and (e) heater T_5. The working fluid was 1.5 cSt silicone oil.

were numerically predicted within 10%. However, the numerical model significantly underpredicted the temperature swings ΔT_i. Here also, discrepancies at locations 1 and 5 can be explained by geometric differences in the simulated heater and cold heat exchanger compared with the experimental device, as previously discussed. An additional source of discrepancy was the fact that experimentally the piston oscillations were not perfectly sinusoidal. This was apparent in the experimental data shown in Figs. 3 and 4. It is likely to have a stronger effect on the local velocity

profile and convective heat transfer coefficient achieved with 1.5 cSt silicone oil than with 50 cSt silicone oil. Moreover, thermophysical properties of the working fluid (e.g., μ_f, $c_{p,f}$, and k_f) depend on temperature. However, this was ignored in our simulations and may also explain the discrepancies. This could be exacerbated by the fact that the temperature oscillations achieved experimentally with 1.5 cSt silicone oil were larger than those obtained for 50 cSt silicone oil. Note also that numerically accounting for the temperature-dependent properties will

Table 4
Computed and experimentally measured average temperatures $\overline{T}_i$ and temperature swings ΔT_i at locations 1 to 5 and relative and absolute error for device operated with 50 cSt silicone oil at different frequencies [12].

	T_1	T_2	T_3	T_4	T_5
f = 0.025 Hz					
Numerical $\overline{T}$ (°C)	47.0	68.9	77.1	85.1	105.1
Experimental $\overline{T}$ (°C)	56.5	70.5	74.5	77.4	89.0
Relative error (%)	16.8	2.3	3.5	9.9	18.1
Numerical ΔT (°C)	21.1	26.0	26.1	25.3	19.2
Experimental ΔT (°C)	37.1	18.3	23.1	23.1	26.1
Absolute error (±°C)	15.9	7.7	3.0	2.2	6.9
f = 0.035 Hz					
Numerical $\overline{T}$ (°C)	50.2	67.3	73.4	79.5	94.6
Experimental $\overline{T}$ (°C)	57.8	71.4	74.7	77.1	87.1
Relative error (%)	13.1	5.7	1.7	3.1	8.6
Numerical ΔT (°C)	17.2	19.6	19.8	18.8	14.9
Experimental ΔT (°C)	39.0	15.0	20.5	20.6	23.7
Absolute error (±°C)	21.8	4.6	0.7	1.8	8.8
f = 0.061 Hz					
Numerical $\overline{T}$ (°C)	58.5	71.4	75.7	79.8	90.9
Experimental $\overline{T}$ (°C)	63.2	76.0	78.5	80.5	89.7
Relative error (%)	7.4	6.1	3.6	0.9	1.3
Numerical ΔT (°C)	14.5	13.4	13.6	12.6	11.7
Experimental ΔT (°C)	34.1	12.2	18.2	19.0	17.9
Absolute error (±°C)	19.6	1.2	4.6	6.4	6.2
f = 0.082 Hz					
Numerical $\overline{T}$ (°C)	62.3	73.1	76.4	79.7	89.0
Experimental $\overline{T}$ (°C)	64.8	76.7	78.5	80.3	88.2
Relative error (%)	3.9	4.6	2.7	0.7	0.9
Numerical ΔT (°C)	12.9	10.4	10.7	9.8	10.3
Experimental ΔT (°C)	31.1	11.1	16.3	17.8	16.1
Absolute error (±°C)	18.2	0.7	5.6	8.0	5.8

Table 5
Computed and experimentally measured average temperatures $\overline{T}_i$ and temperature swings ΔT_i at locations 1 to 5 and relative and absolute error for device operated with 1.5 cSt silicone oil at different frequencies [28].

	T_1	T_2	T_3	T_4	T_5
f = 0.04 Hz					
Numerical $\overline{T}$ (°C)	48.2	62.9	67.7	72.4	85.1
Experimental $\overline{T}$ (°C)	46.1	55.1	68.8	71.0	85.8
Relative error (%)	4.6	14.3	1.6	2.0	0.8
Numerical ΔT (°C)	15.5	15.1	15.3	14.5	13.3
Experimental ΔT (°C)	30.0	34.3	34.9	32.5	21.7
Absolute error (±°C)	14.5	19.2	19.5	18.0	8.4
f = 0.053 Hz					
Numerical $\overline{T}$ (°C)	46.5	61.0	65.5	69.9	82.2
Experimental $\overline{T}$ (°C)	45.8	55.9	68.4	70.4	83.4
Relative error (%)	1.6	9.1	4.2	0.6	1.2
Numerical ΔT (°C)	16.4	14.0	14.2	13.4	13.9
Experimental ΔT (°C)	31.1	31.6	31.1	28.6	21.2
Absolute error (±°C)	14.7	17.6	16.9	15.2	7.2
f = 0.069 Hz					
Numerical $\overline{T}$ (°C)	52.2	65.4	69.3	73.2	84.6
Experimental $\overline{T}$ (°C)	49.2	59.4	72.3	72.9	88.0
Relative error (%)	6.2	10.1	4.2	1.0	3.9
Numerical ΔT (°C)	15.6	12.1	12.2	11.6	13.6
Experimental ΔT (°C)	33.8	31.7	32.0	29.1	25.6
Absolute error (±°C)	18.2	19.5	19.8	17.5	12.5
f = 0.123 Hz					
Numerical $\overline{T}$ (°C)	57.7	66.5	69.0	71.5	80.1
Experimental $\overline{T}$ (°C)	52.2	60.4	70.0	70.7	81.7
Relative error (%)	10.4	10.2	1.4	1.2	1.9
Numerical ΔT (°C)	11.8	7.1	7.5	7.1	11.7
Experimental ΔT (°C)	27.8	24.0	23.8	22.1	23.0
Absolute error (±°C)	15.9	16.9	16.4	15.0	11.3

significantly increase the computational cost and was not possible with the above mentioned hardware (8×2.50 GHz CPUs with 28 GB of RAM).

4.2. Effect of frequency

The numerical model was validated for different operating frequency set at 0.025, 0.035, 0.061, and 0.082 Hz for 50 cSt silicone oil and at 0.04, 0.053, 0.069, and 0.123 Hz for 1.5 cSt silicone oil. Tables 4 and 5 summarize the numerically predicted and experimentally measured mean temperatures $\overline{T}_i$, temperature swings ΔT_i, and their relative differences for each frequency for 50 cSt and 1.5 cSt silicone oil, respectively. Here also, good agreement was found between numerical predictions and experimental results for $\overline{T}_i$ at all locations for both working fluids and at all frequencies considered. However, the numerical model tended to underestimate ΔT_i at all thermocouple locations. The differences for ΔT_i between numerical predictions and experimental data were particularly large for 1.5 cSt silicone oil as previously discussed. Overall, differences between experimental and numerical results did not show any obvious dependence on frequency.

Let us now turn our attention to temperature $T_3(t)$ located in the middle of the PE since it was experimentally monitored to ensure the PE experienced the ferroelectric-to-paraelectric phase transition [12]. Table 6 compares the values of $T_{3,min}$ and $T_{3,max}$ predicted numerically with those obtained experimentally for different piston frequencies and for both 50 cSt and 1.5 cSt silicone oils. Results indicate that the experimental results for $\overline{T}_3$ (Tables 4 and 5), $T_{3,min}$, and $T_{3,max}$ were all numerically predicted within 6% for 50 cSt silicone oil and within 17% for 1.5 cSt silicone oil over the frequency range considered. Additionally, the numerical predictions for ΔT_3 for these frequencies were all within ±6 °C for 50 cSt silicone oil (Table 4) and ±20 °C for 1.5 cSt silicone oil (Table 5). More importantly for pyroelectric energy conversion, the numerically

Table 6
Computed and experimentally measured minimum $T_{3,min}$ and maximum $T_{3,max}$ temperatures versus frequency for 50 and 1.5 cSt silicone oils [12,28].

Frequency	50 cSt silicone oil			
	0.025 Hz	0.035 Hz	0.061 Hz	0.082 Hz
Numerical $T_{3,min}$ (°C)	64.0	63.5	68.8	71.1
Experimental $T_{3,min}$ (°C)	63.0	64.5	69.4	70.3
Relative error (%)	1.7	1.4	0.8	1.1
Numerical $T_{3,max}$ (°C)	90.1	83.3	82.5	81.8
Experimental $T_{3,max}$ (°C)	86.1	84.9	87.6	86.7
Relative error (%)	4.7	1.8	5.8	5.7
	1.5 cSt silicone oil			
	0.040 Hz	0.053 Hz	0.069 Hz	0.123 Hz
Numerical $T_{3,min}$ (°C)	60.1	58.4	63.2	65.3
Experimental $T_{3,min}$ (°C)	51.4	52.9	56.3	58.0
Relative error (%)	16.9	10.5	12.2	12.4
Numerical $T_{3,max}$ (°C)	75.4	72.6	75.4	72.7
Experimental $T_{3,max}$ (°C)	86.3	84.0	88.3	81.9
Relative error (%)	12.6	13.5	14.6	11.2

predicted values of ΔT_3 decreased as the frequency increased, as observed experimentally. This can be attributed to thermal inertia of both the working fluid and the pyroelectric element [12]. As the frequency increased, there was less time for thermal energy to be exchanged between the heating band and the oscillating working fluid and between the working fluid and the pyroelectric elements.

Given the complexity of the experimental apparatus, the numerical predictions for $\overline{T}_3$ and ΔT_3 with 50 cSt silicone oil were in good agreement with experimental data [12]. Similarly, predictions for $\overline{T}_3$ obtained with 1.5 cSt silicone oil were in good agreement with experimental data at all frequencies. However, here also discrepancies were observed for ΔT_3.
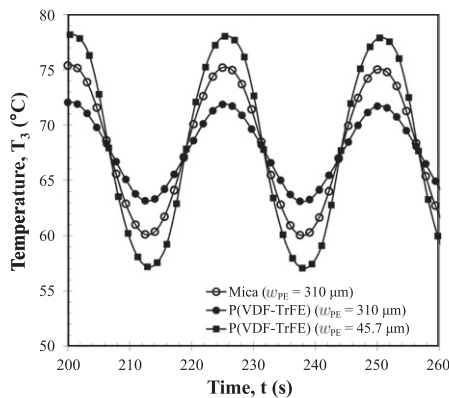
Fig. 5. Numerical predictions of temperature T_3 as a function of time for frequency $f = 0.04$ Hz for a microchannel with (i) a mica plate of thickness $w_{PE} = 310$ μm, (ii) a P(VDF-TrFE) film of same thickness, and (iii) a thinner P(VDF-TrFE) film of thickness $w_{PE} = 45.7$ μm. The working fluid was 1.5 cSt silicone oil.

4.3. Pyroelectric element temperature

Experimental measurements of the temperature of the P(VDF-TrFE) pyroelectric element placed inside the device were not possible due to the inherent risk of the thermocouple discharging and/or short circuiting the PE. As a result, experimental temperature measurements were taken in an adjacent channel along a mica plate inserted in place of the PE. Since good agreement was found between the numerical model and experimental device for the local temperature at location 3, the numerical model can be used to predict the PE temperature that could not be measured experimentally. This can provide predictions for T_{cold} and T_{hot} characterizing the Olsen cycle (Fig. 1) and enable the proper implementation of the cycle and control of the device.

Fig. 5 compares the evolution of temperature T_3 at frequency $f = 0.04$ Hz for a microchannel with (i) a mica plate of thickness $w_{PE} = 310$ μm, (ii) a P(VDF-TrFE) film of same thickness, and (iii) a thinner P(VDF-TrFE) film of thickness $w_{PE} = 45.7$ μm as experimentally used by Nguyen et al. [12]. Here, the working fluid was 1.5 cSt silicone oil. Fig. 5 indicates that the average temperature $\overline{T}_3$ remained nearly unchanged regardless of material and thickness. However, the temperature swing ΔT_3 increased by 5 °C when replacing the mica with a P(VDF-TrFE) film of identical thickness. It further increased by 12 °C when reducing the P(VDF-TrFE) film thickness w_{PE} from 310 μm to 45.7 μm. Similar results were observed for $\overline{T}_i$ and ΔT_i at locations 2, 3, and 4 as well as when simulating 50 cSt silicone oil. This can be explained by the fact that the thermal mass of a P(VDF-TrFE) film (i) was smaller than that of a mica plate of same thickness and (ii) decreased with decreasing thickness. However, $T_1(t)$ (cold heat exchanger) and $T_5(t)$ (heater) remained nearly unchanged by replace mica with P(VDF-TrFE) and/or decreasing the film thickness.

Finally, the electrocaloric effect refers to the change in temperature in a material upon application and withdrawal of an electric field under adiabatic conditions. For example, Neese et al. [25] estimated a change in temperature of 4 °C and 12 °C when 55/45 P(VDF-TrFE) films were subject to an electric field cycled between ±134 and ±209 MV/m, respectively. Similarly, Liu et al. [26] estimated adiabatic temperature change of 4 °C and 21 °C as electric field applied to 70/30 P(VDF-TrFE) films was cycled between ±100 and ±300 MV/m, respectively. Thus, the electrocaloric effect could affect the temperature swing experienced by the PE as it underwent the Olsen cycle. However, in our pyroelectric energy conversion experiments using 60/40 P(VDF-TrFE) films [12,27], the maximum electric field ranged between 20 and 60 MV/m.

Therefore, the electrocaloric effect could be neglected in the simulations of our pyroelectric energy converter.

5. Conclusion

This study aimed to further develop and to validate a simulation tool by comparing numerical predictions with experimental results collected on an instrumented prototypical pyroelectric energy converter using 50 cSt or 1.5 cSt silicone oils as working fluid and operating at various frequencies [12]. Numerical simulations predicted that the temperature swing ΔT_i decreased with operating frequency as observed experimentally. Numerical predictions for the mean temperature at the five locations within the device showed good agreement with experimental data for both working fluids at all frequencies considered. The temperature swing at those locations was underestimated slightly for 50 cSt silicone oil and significantly more for 1.5 cSt silicone oil. Replacing the mica plate with a P(VDF-TrFE) film of same thickness or thinner resulted in larger temperature swing.

Future work should improve the numerical predictions for temperature swings with low viscosity working fluid. This can be achieved by using temperature-dependent fluid properties and/or accounting for the actual piston dynamics instead of the sinusoidal oscillations simulated in this study. However, this will significantly increase the computational cost of the simulations. This experimentally validated simulation tool confirms our previous predictions [14] and can be used in the design of next generation pyroelectric energy converters based on oscillatory convective heat transfer to maximize the device performance in a cost and time-efficient manner. Experiments should be performed to confirm the design of a pyroelectric energy converter and in particular to finalize the choice of the working fluid.

References

[1] Lawrence Livermore National Laboratory, Estimated U.S. energy use in 2009, <https://flowcharts.llnl.gov/>, September 07, 2011.

[2] B.T. Liu, K.H. Chien, C.C. Wang, Effect of working fluids on organic Rankine cycle for waste heat recovery, Energy 29 (8) (2004) 1207–1217.

[3] D.G. Thombare, S.K. Verma, Technological development in the Stirling cycle engines, Renew. Sust. Energy Rev. 12 (2008) 1–38.

[4] S.B. Riffat, X. Ma, Thermoelectrics: a review of present and potential applications, Appl. Therm. Eng. 23 (2003) 913–935.

[5] R.B. Olsen, D.A. Bruno, J.M. Briscoe, W.F. Butler, A pyroelectric energy converter which employs regeneration, Ferroelectrics 38 (1981) 975–978.

[6] R.B. Olsen, Ferroelectric conversion of heat to electrical energy – a demonstration, J. Energy 6 (1982) 91–95.

[7] R.B. Olsen, D.D. Brown, High-efficiency direct conversion of heat to electrical energy related pyroelectric measurements, Ferroelectrics 40 (1982) 17–27.

[8] R.B. Olsen, D.A. Bruno, J.M. Briscoe, Cascaded pyroelectric energy converter, Ferroelectrics 59 (1984) 205–219.

[9] R.B. Olsen, D.A. Bruno, J.M. Briscoe, Pyroelectric conversion cycles, J. Appl. Phys. 58 (1985) 4709–4716.

[10] R.B. Olsen, D.A. Bruno, J.M. Briscoe, Pyroelectric conversion cycle of vinylidene fluoride–trifluoroethylene copolymer, J. Appl. Phys. 57 (1985) 5036–5042.

[11] G. Sebald, S. Pruvost, D. Guyomar, Energy harvesting based on Ericsson pyroelectric cycles in a relaxor ferroelectric ceramic, Smart Mater. Struct. 17 (2008) 15012.

[12] H. Nguyen, A. Navid, L. Pilon, Pyroelectric energy converter using co-polymer P(VDF-TrFE) and Olsen cycle for waste heat energy harvesting, Appl. Therm. Eng. 30 (2010) 2127–2137.

[13] A. Navid, D. Vanderpool, A. Bah, L. Pilon, Towards optimization of a pyroelectric energy converter for harvesting waste heat, Int. J. Heat Mass Transfer 53 (2010) 4060–4070.

[14] D. Vanderpool, J.H. Yoon, L. Pilon, Simulations of a prototypical device using pyroelectric materials for harvesting waste heat, Int. J. Heat Mass Transfer 51 (21-22) (2008) 5052–5062.

[15] J.A. Gonzalo, Ferroelectric materials as energy converters, Ferroelectrics 11 (1976) 423–430.

[16] R.B. Olsen, W.F. Butler, J.E. Drummond, D.A. Bruno, J.M. Briscoe, Heat flow in a pyroelectric converter, in: 20th Intersociety Energy Conservation Engineering Conference, vol. 3, 1985, pp. 595–602.

[17] R. Kandilian, A. Navid, L. Pilon, The pyroelectric energy harvesting capabilities of PMN-PT near the morphotropic phase boundary, Smart Mater. Struct. 20 (1) (2011) 055020.

[18] F.Y. Lee, A. Navid, L. Pilon, Pyroelectric waste heat energy harvesting using heat conduction, Appl. Therm. Eng. 37 (1) (2012) 30–37.

[19] I.M. McKinley, R. Kandilian, L. Pilon, Waste heat energy harvesting using Olsen cycle on $0.945Pb(Zn_{1/3}Nb_{2/3})O_3$–$0.055PbTiO_3$ single crystals, Smart Mater. Struct. 21 (3) (2012) 035015.

[20] A. Bejan, Convection Heat Transfer, John Wiley and Sons, New York, NY, 2004.

[21] Dow Corning Corp., Dow Corning 200® Fluid, 50 cst and 1.5 cst Product Information Sheet, <http://www.dowcorning.com>, May 20, 2009.

[22] K.M. Krupka, High-temperature heat capacities of corundum, periclase, anorthite, $CaAl_2Si_2O_8$ glass, muscovite, pyrophillite, $KAlSi_3O_8$ glass, grossular, and Na $AlSi_3O_8$ glass, Amer. Mineral. 64 (1979) 86–101.

[23] A. Navid, C.S. Lynch, L. Pilon, Purified and porous poly (vinylidene fluoride–trifluoroethylene) [P(VDF-TrFE)] thin films for pyroelectric infrared sensing and energy harvesting, Smart Mater. Struct. 19 (2010) 055006.

[24] Y.W. Wong, N.M. Hui, E.L. Ong, H.L.W. Chan, C.L. Choy, Specific heat and thermal diffusivity of vinylidene fluoride/trifluoroethylene copolymers, J. Appl. Polym. Sci. 89 (2003) 3160–3166.

[25] B. Neese, B. Chu, S.-G. Lu, Y. Wang, E. Furman, Q.M. Zhang, Large electrocaloric effect in ferroelectric polymers near room temperature, Science 321 (821) (2008) 1159655.

[26] P.F. Liu, J.L. Wang, X.J. Meng, J. Yang, B. Dkhil, J.H. Chu, Huge electrocaloric effect in LangmuirBlodgetts ferroelectric polymer thin films, New J. Phys. 12 (2010) 023035.

[27] A. Navid, L. Pilon, Pyroelectric energy harvesting using Olsen cycles in purified and porous poly (vinylidene fluoride–trifluoroethylene) thin films, Smart Mater. Struct. 20 (2) (2011) 025012.

[28] H. Nguyen, Pyroelectric energy converter using co-polymer P(VDF-TrFE) and Olsen cycle for waste heat energy harvesting, Master's thesis, University of California, Los Angeles, 2010.

[29] McMaster-Carr, Natural muscovite mica information sheet, <http://www.mcmaster.com>, 2009.

[30] Attwater Group, Product data sheet for attamica H, integrated mica, <http://www.attwater.com>, September 07, 2011.